

Evolution of ordered nanoporous phases during h-BN growth: Controlling the route from gas-phase precursor to 2D material by *in-situ* monitoring.

Adrian Ruckhofer,[†] Marco Sacchi,[‡] Anthony Payne,[‡] Andrew P. Jardine,[¶] Wolfgang E. Ernst,[†] Nadav Avidor,^{*,¶} and Anton Tamtögl^{*,†}

[†]Institute of Experimental Physics, Graz University of Technology, Graz, Austria

[‡]Department of Chemistry, University of Surrey, Guildford GU2 7XH, United Kingdom

[¶]Cavendish Laboratory, J. J. Thompson Avenue, Cambridge CB3 0HE, United Kingdom

E-mail: nadavavidor@gmail.com; tamtoegl@gmail.com

ABSTRACT: Large-area single-crystal monolayers of two-dimensional (2D) materials such as graphene and hexagonal boron nitride (h-BN) can be grown by chemical vapour deposition (CVD). However, the high temperatures and fast timescales at which the conversion from a gas-phase precursor to the 2D material appear, make it extremely challenging to simultaneously follow the atomic arrangements. We utilise helium atom scattering to discover and control the growth of novel 2D h-BN nanoporous phases during the CVD process. We find that prior to the formation of h-BN from the gas-phase precursor, a metastable (3×3) structure is formed, and that excess deposition on the resulting 2D h-BN leads to the emergence of a (3×4) structure. We illustrate that these nanoporous structures are produced by partial dehydrogenation and polymerisation of the borazine precursor upon adsorption. These steps are largely unexplored during the synthesis of 2D materials and we unveil the rich phases during CVD growth. Our results provide significant foundations for 2D materials engineering in CVD, by adjusting or carefully controlling the growth conditions and thus exploiting these intermediate structures for the synthesis of covalent self-assembled 2D networks.

Introduction

Two-dimensional (2D) materials such as graphene and hexagonal boron nitride (h-BN) offer technological promise^{1,2}, e.g. with h-BN being considered to be the “ideal” dielectric for 2D based field-effect transistors³. However, their properties are highly dependent on the perfection of the 2D layers. For this reason, intense efforts have been devoted to study and improve the growth of defect-free 2D materials.^{4,5} A promising method of synthesising large-area 2D layers is chemical vapour deposition (CVD) and the CVD synthesis of atomically thin h-BN on metal substrates is described in several review articles.^{6,7} The process, which is illustrated in Figure 1, involves a gas-phase precursor deposited on a solid substrate at elevated temperatures. By diffusion and dehydrogenation or fragmentation of the precursor, the adsorbates are attached to growing clusters and eventually form the 2D layer. A complete dehydrogenation of the precursor requires overcoming multiple energy barriers. As a result, it might be expected that at intermediate temperatures, dehydrogenation would not be complete, which in-turn can result in metastable or intermediate structures. For the synthesis of bulk h-BN it is known that the process involves several steps of borazine-polymerisation.^{8–11}

There are several routes, but even in the bulk the process has not been studied in great detail. Here, we follow a series of structural changes to identify intermediate structures in 2D growth.

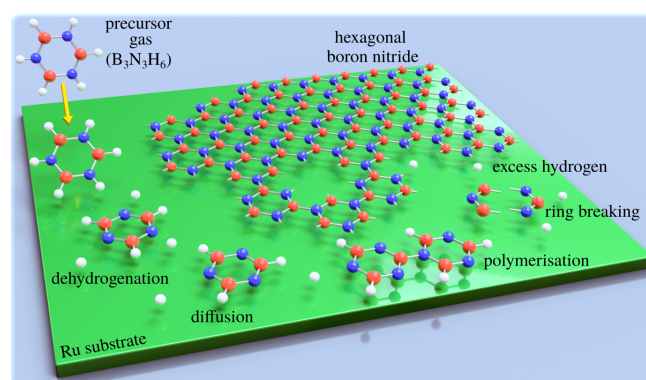


Figure 1: Schematic illustrating the epitaxial growth of h-BN by chemical vapour deposition: A gaseous precursor (e.g. borazine, $B_3N_3H_6$) is brought into contact with a (hot) catalyst surface (Ru), triggering the chemical reactions such as breaking of the borazine rings and dehydrogenation, followed by the assembly of the epitaxial overlayer.

While it is crucial to understand the growth process, mechanistic and kinetic studies are rare and mostly focus on the growth of nanocarbons.^{12–15} Dehydro-

generation and intermediate structures during CVD of 2D materials have been proposed,^{16–22} but to the best of our knowledge have not been studied experimentally. In general, kinetics and the thermochemistry of intermediate products, may lead to metastable structures. However, phase-diagrams due to partially dehydrogenated precursors have not been reported. Most studies report completed overlayer structures while the complexity and individual steps, as illustrated in Figure 1, are often ignored. In particular, previous h-BN studies using real space methods^{23–26} concentrate on local order in completed h-BN structures, while reciprocal space studies^{27–29} have provided information about long-range order.³⁰

In this paper we present a systematic analysis, at various temperatures beyond the ones reported for best growth conditions (1050 K–1100 K^{23,25,28}) and at various dosing rates. By following h-BN growth *in situ* using helium atom scattering (HAS) we demonstrate the existence of metastable structures during the formation of h-BN from borazine ($\text{B}_3\text{N}_3\text{H}_6$). HAS is a well-established technique for monitoring thin-film growth modes^{31–33} and has been used to study the quality of CVD-grown 2D materials^{34–37} and inter-layer interaction,³⁸ yet investigations of intermediate structures have not been performed. In particular, we find that there is one precursor structure with a well-defined (3×3) periodicity, meaning a well-defined route for the polymerisation reaction which leads to h-BN. We further find that by dosing excess borazine, a (3×4) structure forms, which could be attributed to a partially polymerised second-layer on top of the formed h-BN.

Our experimental results are complemented by van der Waals (vdW) corrected density functional theory (DFT) calculations which confirm the nature of the system, helping us to determine which self-assembled structures are compatible with the experimental results.

Results and Discussion

The adsorption of the precursor gas (borazine, $\text{B}_3\text{N}_3\text{H}_6$) on the Ru substrate has been investigated in several other studies using Auger electron spectroscopy, X-ray photoelectron spectroscopy, electron energy loss spectroscopy and low energy electron diffraction.^{39–41} There is general consensus in the literature, that borazine only adsorbs molecularly at low (140 K) temperatures^{40–42} with dehydrogenation setting in at temperatures of 150–250 K, depending on the substrate.^{40,41,43} Starting from about 600 K, again depending on the metallic substrate, the B–N ring is reported to break down into its atomic constituents.^{42,43} According to Paffet *et al.* 1000 K are necessary for h-BN formation on Ru(0001)^{39,40} while hydrogen desorption occurs over a wide temperature range⁴¹

and may even intercalate in the h-BN layer.^{44,45}

Helium diffraction allows *in situ* measurements even at growth temperature, and is known for its unique sensitivity to adsorbates, including hydrogen atoms.^{46–54} Furthermore, unlike other established techniques,⁵⁵ HAS is completely inert and does not modify the process under investigation.⁵⁶ While the specular reflection gives an estimate of adsorbate coverage on the clean surface, the angular distribution provides insight in the time evolution of periodic structures being formed on the surface.^{30,35} In the present work, CVD growth was performed at a set crystal temperature while monitoring the surface using repeated one-dimensional angular diffraction scans, where we observe the emergence and disappearance of additional superstructures followed by the formation of h-BN.

All experimental data was obtained with the Cambridge spin-echo apparatus which uses a nearly monochromatic atomic beam of ^3He , scattered off the sample in a total scattering angle of 44.4° and with an incident energy of 8 meV (see Experimental Section in the Supporting Information). The parallel momentum transfer ΔK is given by $\Delta K = |\Delta \mathbf{K}| = |\mathbf{K}_f - \mathbf{K}_i| = |\mathbf{k}_i| (\sin \vartheta_f - \sin \vartheta_i)$, with \mathbf{k}_i being the incident wavevector and ϑ_i and ϑ_f the incident and final angles with respect to the surface normal, respectively.^{57–59} Compared to techniques such as scanning tunnelling microscopy (STM), HAS averages over larger surface areas, typically $\approx 3 \text{ mm}^2$. Therefore, the advantage of HAS is to give precise information about any long-range periodicity of surface structures. For ease of comparison, the diffraction scans for the different structures are plotted as a function of the parallel momentum transfer, ΔK , relative to the G_{01} peak of the Ru(0001) substrate, $|\Delta K/G_{01}|$. By converting the abscissa in this way, the position of the observed diffraction peaks directly reflects their periodicity with respect to the substrate lattice spacing.

A precursor structure to h-BN growth

First, we describe how borazine exposure at low temperature ($T < 880 \text{ K}$) reveals a precursor structure on Ru(0001), which by further annealing at $T = 880 \text{ K}$ can be converted to h-BN.

The purple line in Figure 2(a) shows a diffraction scan of the clean Ru(0001) substrate. Exposing Ru to 7 Langmuir (L) of borazine at a surface temperature of 600 K, results in decreased diffraction intensities and helium reflectivity. Moreover, the lack of any additional diffraction peaks is typical of a disordered structure.⁵⁴ The behaviour is consistent with earlier studies showing that the B–N ring starts to break down into its constituents only above about 600 K.^{39,42,43}

Upon increasing the temperature to 750 K while maintaining borazine overpressure, additional peaks start to appear between the specular and first order Ru diffraction peaks. Figure 2(b) (blue curve) shows the

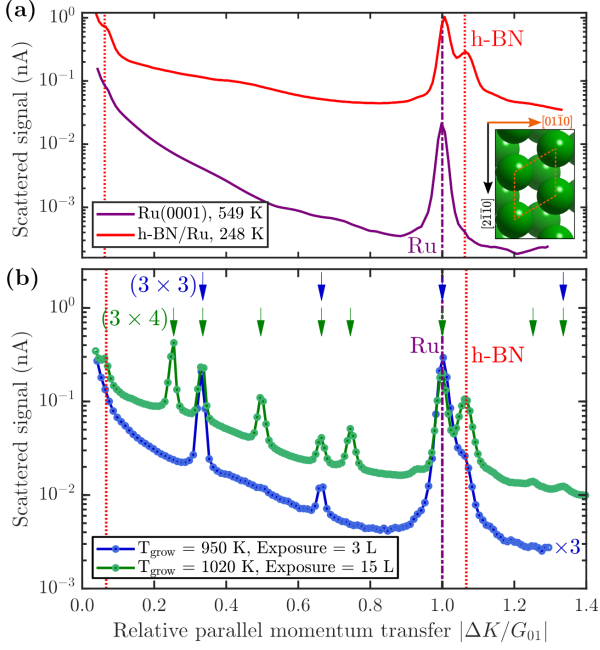


Figure 2: (a) Comparison of the angular diffraction scans for clean Ru(0001) in purple and the completed h-BN overlay on Ru in red. The $\langle 01\bar{1}0 \rangle$ scanning direction ($\bar{\Gamma}\bar{M}$) is shown in the inset. The purple dash-dotted line indicates the position of the first order Ru diffraction peak and the red dotted lines the h-BN Moiré peaks. (b) Diffraction scans during borazine exposure reveal additional superstructures, depending on the growth temperature and total exposure. The position (shown by the arrows at the top) and spacing of the additional peaks reveal a $(3 \times 3) / (3 \times 4)$ superstructure plotted in blue / green. Low exposure at lower temperatures reveals a (3×3) structure (blue curve, grown at 950 K), while at higher exposures and higher temperatures an intermediate (3×4) pattern emerges (green curve, grown at 1020 K). To improve the signal to noise ratio, the sample was subsequently cooled down for the duration of both scans and the blue curve was scaled by a factor of 3 to facilitate comparison.

characteristic diffraction pattern that emerges. Equidistant peaks at $|\Delta K/G_{01}| = 0.33$ and 0.66 indicate a (3×3) periodic structure on the surface, which we label BN_I . If dosing is performed at even higher temperatures ($T \geq 880$ K), in addition to the observed BN_I structure, a shoulder appears to the right-hand side of the first order Ru diffraction peak, indicating the formation of a h-BN structure on the surface (vertical red dotted line in Figure 2). The peak, which occurs at $|\Delta K/G_{01}| = 1.08$, is a result of the commensurate Moiré pattern on Ru²⁸ (see also h-BN periodicity in the SI).

Since a (3×3) superstructure composed of intact borazine molecules shows only weak binding to the substrate, the observed BN_I structure, as shown later in our DFT calculations, must be composed of partly dehydrogenated borazine molecules, in line with the reported low experimental dehydrogenation temperature on other substrates.⁴³ Figure 3 illustrates *in*

situ monitoring of the integrated peak intensities, which demonstrates that the BN_I structure precedes the growth of h-BN. The exposure dependent intensities are obtained from repeated angular diffraction scans. Immediately after dosing begins, the (3×3) peaks start to rise rapidly (blue line), while only after a short delay the h-BN diffraction peak increases (red line), although less quickly than the BN_I structure. The h-BN peak intensity reaches its maximum at the same point where the BN_I structure disappears. We conclude that the BN_I structure is converted into h-BN and acts as a precursor structure to the complete h-BN overlayer. Since the intensity of the BN_I structure drops to almost zero at ≈ 9 L, it indicates that virtually all (3×3) domains are converted to h-BN.

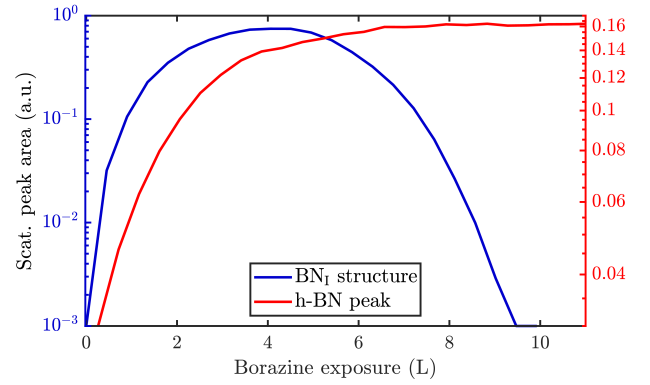


Figure 3: *In situ* monitoring of the integrated peak intensities reveals that the BN_I structure acts as precursor to the h-BN overlayer. The characteristic diffraction peaks for the BN_I structure and the h-BN peak are plotted versus borazine exposure at a substrate temperature of 880 K. The BN_I structure increases prior to the h-BN intensity and has already disappeared when the h-BN intensity exhibits its maximum.

The temperature region where the BN_I structure evolves is in excellent agreement with the desorption temperature of hydrogen reported by Paffett *et al.*,³⁹ which helps confirm the dehydrogenation process. Further, as mentioned earlier, bulk h-BN is known to form by a sequence of dehydrogenation processes, in which borazine polymerises to polyborazylene, which is then cross-linked in one or more steps.^{9,10} Our results suggest that a similar process happens at the ruthenium surface, but that in the 2D case, there is one clear intermediate step, i.e. the BN_I structure, before the formation of h-BN. There are several possible real space structures, which are in line with the observed periodicity and composition²². We concentrate on providing experimental proof that such intermediate / precursor structures with long-range order exist, while the exact chemical composition of these structures is better probed with X-ray photoemission spectroscopy (XPS) studies⁴⁰, beyond the mentioned structural analysis. Moreover, the precursor gas imposes a B/N ratio of 1:1 which we do not expect to change and we have therefore focussed on supporting our structural characteri-

sation through detailed DFT modelling of appropriate candidate structures.

DFT structural modelling

We understand the BN_I structure to consist of partially dehydrogenated, polymerised borazine analogous to the synthesis of bulk h-BN. Thus it is apparent that the 2D growth occurs in a step-by-step process and that not all hydrogen atoms are expected to be removed at the same time, due to the different bonding strengths to N and B atoms, as well as the bond formation between the N and the Ru atoms. Based on this attribution, we have made a vdW-corrected DFT investigation into the energetics of the BN_I structure, from adsorption of the precursor gas to the complete h-BN overlayer.

We start by considering a single borazine molecule in a (3×3) supercell (see Computational Methods in the Supporting Information), and move on to partially dehydrogenated borazine polymers. From the adsorption energies of isolated borazine molecules we observe that the bonding becomes much stronger with dehydrogenation, but the calculations cannot provide a definitive answer in terms of the dehydrogenation sequence (dehydrogenation of the B atoms is slightly more favourable than of the N atoms by ≈ 15 meV). However, as shown later for two borazine molecules per supercell, the N atoms can dehydrogenate more easily than the B atoms and the candidate structures for our observations can be clearly distinguished in terms of the adsorption energies.

Table 1: DFT calculations for the adsorption structures of the borazine precursor on Ru(0001), based on one molecule per (3×3) supercell. The results are shown for an intact ($\text{B}_3\text{N}_3\text{H}_6$) and partially dehydrogenated ($\text{B}_3\text{N}_3\text{H}_3$) adsorbate, considering various initial adsorption sites and a rotation of 60° (see Figure 4(a)). The adsorption energies E_{ads} are given for the final optimised adsorption sites and ΔE is the difference with respect to the minimum energy configuration of the system with the same dehydrogenation state.

$\text{B}_3\text{N}_3\text{H}_6$			$\text{B}_3\text{N}_3\text{H}_3$		
Site	E_{ads} (eV)	ΔE (eV)	Site	E_{ads} (eV)	ΔE (eV)
fcc	-4.08	0.00	fcc	-8.95	0.00
top	-1.21	2.86	top	-6.60	2.35
b \rightarrow fcc	-4.08	0.00	b \rightarrow fcc	-8.95	0.00
hcp	-1.31	2.77	hcp	-5.88	3.07

In Table 1 we compare the binding energies from vdW-corrected DFT for an intact ($\text{B}_3\text{N}_3\text{H}_6$) and a partially dehydrogenated ($\text{B}_3\text{N}_3\text{H}_3$) borazine molecule with one molecule per (3×3) supercell, confirming a much stronger bonding of $\text{B}_3\text{N}_3\text{H}_3$. We consider various initial adsorption sites (Figure 4(a)) with respect to the C_3 rotational axis through the centre of

the molecule and a rotation of 60° . Adsorption occurs in a flat face-to-face configuration, while bonding of the same adsorbates with a rotation of 0° is slightly weaker – the results are shown in the Supplementary Information (see Supplementary DFT calculations).

In Table 1 the energy differences ΔE are given with respect to the minimum energy of the same dehydrogenation state in addition to the respective adsorption energies E_{ads} . For both stoichiometric configurations the most favourable position is the fcc site and if the borazine molecule is initially placed on a bridge site it undergoes a transition to this position. The fcc configuration for partially dehydrogenated borazine yields an adsorption energy of $E_{\text{ads}} = -8.95$ eV and is shown in Figure 4(a) with the (3×3) supercell highlighted by the black dashed rhombus. The results for the intact borazine molecule ($\text{B}_3\text{N}_3\text{H}_6$) are very similar with respect to the adsorption site, however, we obtain significantly weaker bonding strengths compared to the dehydrogenated molecule.

Based on bulk h-BN studies we conclude that it is more likely that polymerised networks are formed.^{9,10} Starting from the minimum energy configuration of a single borazine molecule on the fcc site we continue by adding a second borazine molecule in the supercell. By considering various initial rotations of the additional molecule the energetically most favourable configurations were then identified. In contrast to the case of an isolated borazine molecule, the dehydrogenation sequence becomes clearly discernible in terms of the adsorption energies, with two borazine molecules. The N atoms in the ring adsorb on top of the Ru atoms and the borazine molecules lose all hydrogen atoms associated with the N atoms upon bond formation, in line with experimental results of the completed h-BN overlayer where inter-layer bonding is facilitated via the N atoms.^{6,23} Such a scenario is, however, different to bulk h-BN growth where ruthenium is not present and thus interaction with the substrate may give rise to an even faster loss of hydrogen compared to bulk studies.

The calculations for two intact borazine molecules per supercell ($2\text{B}_3\text{N}_3\text{H}_6$, not shown) yield weak binding, since the H atoms start to overlap resulting in a tilt of the complete molecules with respect to the surface. Moreover, due to desorption of hydrogen atoms from the borazine at low temperatures it is unlikely that intact borazine will remain and so intact molecules will not be considered further.³⁹

Therefore, we concentrate on partially and fully dehydrogenated borazine molecules. Figure 4(b,c) shows the final optimised structure for $2\text{B}_3\text{N}_3\text{H}_3$ per supercell, illustrating that individual borazine molecules form bonds to each other. The bound B-N rings build up a nanostructured network with nanopores, i.e. where in between the B-N rings vacancies/pores of the Ru substrate are left behind. The high binding energy of the structure in Figure 4(b) with -6.28 eV compared to

−6.74 eV for the complete h-BN/Ru, may therefore explain the stability of the BN_I structure at temperatures ≈750 K as observed in the experiments.

The structure in Figure 4(b) acts as an intermediate prior to complete dehydrogenation which is expected at elevated temperatures. The calculations show that first the hydrogen atoms detach from the nitrogen and bind to the Ru substrate on the hcp sites, inside the nanopores. The excess hydrogen adatoms inside the nanopores are likely to desorb relatively quickly at the temperature of the experiment.⁶⁰ Therefore, Figure 4(c) shows the optimised structure, starting with two fully dehydrogenated borazine molecules per supercell, leading again to the formation of nanopores. Such an open structure could easily act as a precursor to the complete h-BN overlayer, since each pore only has to be “filled” with an additional dehydrogenated borazine molecule. Finally, the addition of further borazine molecules in the calculations, i.e. three per supercell, essentially leads to the formation of h-BN which gives rise to the strongest binding energy in the calculations. The route from the precursor BN_I structure to the final h-BN overlayer, with several intermediate steps, is illustrated in Supplementary Figure 3.

In addition to providing us with real-space structures of the observed BN_I precursor, there are several points which we note from the vdW DFT calculations: Dehydrogenation of borazine always gives rise to a stronger bonding to the substrate and the results show that the thermodynamically most stable configuration for three adsorbed borazine molecules is h-BN (Supplementary Figure 2(b)). We also see from the side views in Figure 4 that there occurs always some buckling (0.21 – 0.35 Å) and the adlayer is never perfectly flat. The results show that by carefully controlling the substrate temperature and thus the amount of excess hydrogen in future experiments, several BN nano-structures could be synthesized as shown for two cases in Figure 4(b,c). Moreover, careful changes of the starting conditions in the DFT calculations may even yield a “local” minimum energy configuration as in Supplementary Figure 2(c). Thus the system may be an ideal playground for the growth of different nano-structures and further metastable networks beside the ones reported in this work.

Additional structures accompanying the h-BN growth

So far, we have described the formation of a BN_I structure at $T \geq 750$ K, which is converted to h-BN at $T \geq 880$ K. However, upon complete conversion of the BN_I structure to h-BN, exposing the surface to excess borazine results in the emergence of an additional structure with a (3×4) periodicity, which we label BN_{II}. The green line in Figure 2(b) illustrates the corresponding diffraction pattern with the h-BN Moiré diffraction peak being still present next to the first order Ru peak.

As shown in a two-dimensional diffraction scan in Supplementary Figure 5, the (3×4) peaks are not a subset of the h-BN Moiré pattern. In addition, a smaller peak to the left of the first order Ru peak becomes visible which can be attributed to a substrate reconstruction peak²⁸ due to the h-BN growth.

To monitor the growth of the BN_{II} structure we use a smaller borazine overpressure while holding the sample temperature at 915 K. Figure 5(a) shows the evolution of the BN_{II} and the BN_I structure as blue and green curves, respectively. Here, the red line is again the integrated peak intensity of the h-BN diffraction peak. Immediately after exposing the surface to borazine, the BN_I structure increases together with the h-BN peak. Further exposure leads to a decay of the BN_I structure, while the h-BN feature still rises, indicating the growth of h-BN islands. At 7 L the h-BN diffraction peak saturates, while at the same time the BN_I structure disappears. At this stage the h-BN overlayer is complete and after further dosing of borazine, the BN_{II} structure starts to emerge. As discussed later this may be interpreted as a second layer being formed on top of h-BN.

The measurement was repeated at an even lower dosing pressure, while holding the sample at the lower temperature of 880 K. In Figure 5(b) the same behaviour is reproduced, yielding a h-BN layer with two additional structures, except that the emergence is delayed to longer/higher exposures, thus indicating a kinetically driven conversion.

With continuing borazine exposure to 20 L in Figure 5(b), the BN_{II} structure reaches its maximum with no further changes in the scattered intensity. Together with the rise of the BN_{II} structure the h-BN peak intensity slowly starts to decay, likely due to diffuse scattering from additional adsorbates at the surface or from domain walls of the BN_{II} structure. Increasing the surface temperature to 1000 K gives rise to a decay of the BN_{II} structure while the h-BN peak intensity starts to recover to its original value. Further temperature increase accelerates this process giving rise to a faster transition/conversion until the intermediate peaks disappear, leaving behind only the h-BN layer. Such a behaviour illustrates that ultimately h-BN is the most stable structure. Even though the borazine overpressure was still present, no additional peaks formed and the h-BN overlayer is the only remaining structure at the surface.

From Figure 5(b) it becomes evident, that in contrast to the BN_I structure, the BN_{II} structure is much more stable at higher temperatures since the (3×4) diffraction peaks are observed up to 1000 K. Further increase of the temperature to ≈ 1200 K gives rise to the surface migration of bulk-dissolved carbon, leading to the formation of graphene (see Supplementary diffraction scans) and thus eventually destroys the h-BN overlayer. The latter may open up the possibility to study the growth of h-BN/graphene heterostructures^{61–64} but is

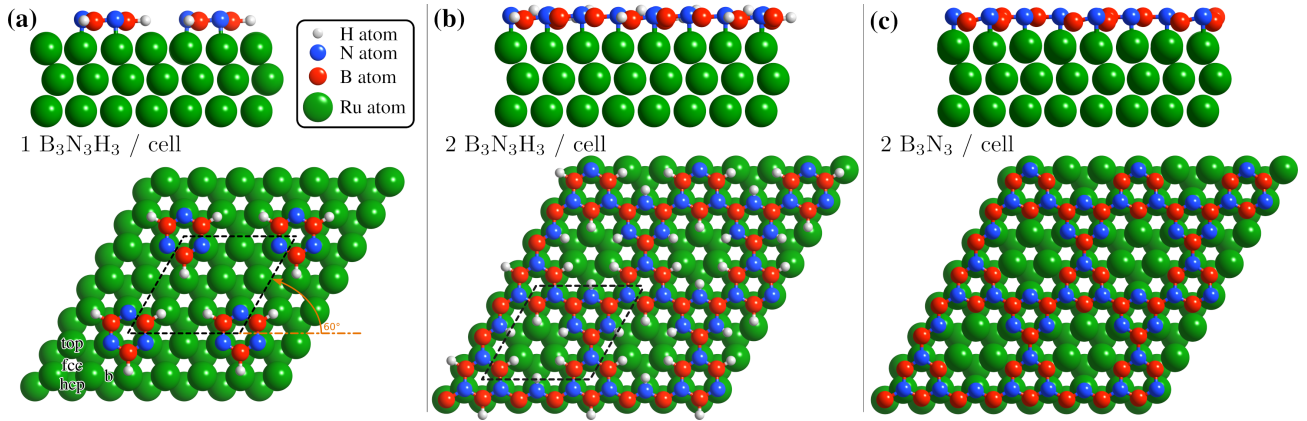


Figure 4: Side and top view of the energetically most favourable configurations on the Ru(0001) surface, from one to two borazine molecules per supercell. (a) For one partially dehydrogenated borazine molecule ($B_3N_3H_3$) adsorption occurs on the fcc site, forming a (3×3) structure. (b) shows the structure for two partially dehydrogenated $B_3N_3H_3$ molecules per supercell, where bound B-N rings form a nanostructured network and hydrogen atoms remain adsorbed on the Ru lattice inside the nanopores. In (c) the optimised structure for two fully dehydrogenated borazine molecules is shown, leading to the same nanopore structure with a (3×3) periodicity.

beyond the scope of the current study.

From our experiments it is likely that the BN_{II} structure is a second chemisorbed layer on top of already grown h-BN. Earlier works on an Ir(111) substrate showed the evolution of additional compact reconstructed regions with a (6×2) superstructure, which were attributed to reconstructed boron areas.⁶⁵ On the other hand, CVD growth on polycrystalline Cu provided evidence for boron dissolution into the bulk together with multilayer h-BN formation via intercalation.⁶⁶ However, both systems and studies are significantly different from our approach. E.g., the different behaviour in the first study could be due to changes of both the lattice constant and the h-BN-substrate bonding between Ru and Ir. Moreover, in light of the recent observation of h-BN multilayer growth³, a second chemisorbed layer is much more plausible.

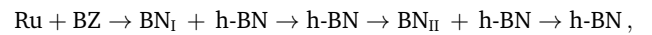
The BN_{II} structure, as a second chemisorbed layer, consists of partly or completely dehydrogenated borazine molecules with a desorption temperature slightly above our performed measurements, since we see an adsorption/desorption equilibrium at temperatures $< \approx 1000$ K with an ultimate desorption at temperatures above this value. The existence of such a structure might be a precursor to multilayer synthesis if the original h-BN layer is of poor quality providing a high density of growth nuclei and thus explaining the reports of multilayer growth.^{3,66–69}

In a set of additional DFT calculations summarised in Supplementary Table 2, we considered also the possibility of borazine adsorption on top of h-BN/Ru as well as the formation of bi-layer h-BN.^{66–69} However, we can rule out the latter according to our deposition measurements, since we do not detect oscillations of the BN_{II} structure or observations of any other periodicity, that would be indicative of multilayer h-BN growth. In line with the multi-stage process of h-BN

bulk formation it is more likely that the BN_{II} structure consists of adsorbed molecules or polymerised borazine structures - with a weaker bonding compared to the first h-BN layer and therefore more likely to desorb. Further unlikely scenarios are discussed in Supplementary discussion.

h-BN growth diagram on Ru(0001)

The combination of measurements and DFT calculations allows us to conclude that the whole system passes through various structural phases:



with the outcome depending strongly on substrate temperature, borazine exposure and the point where one stops. In particular, the surface temperature strongly influences the kinetics and thus the duration and appearance of the additional superstructures. Combining the experimental results we derive a growth diagram as shown in Figure 6, which describes the phenomenology of various structures arising during the CVD growth of h-BN on Ru(0001).

Below 750 K no periodic overlayer structure on the Ru(0001) surface is found. Between 750 and 880 K the BN_I structure forms on the surface which upon further borazine exposure vanishes and leaves a disordered phase behind. The minimum temperature to form a h-BN overlayer on the surface was determined to be 880 K. Above this temperature we observe additional structures, starting with a (3×3) structure (BN_I) followed by a (3×4) periodic diffraction pattern (BN_{II}). These structures always appear in addition to the h-BN layer and ultimately vanish, leaving a complete h-BN overlayer behind (see Figure 2(a) for a diffraction scan of a complete h-BN overlayer without any additional structures). We have thus identified two

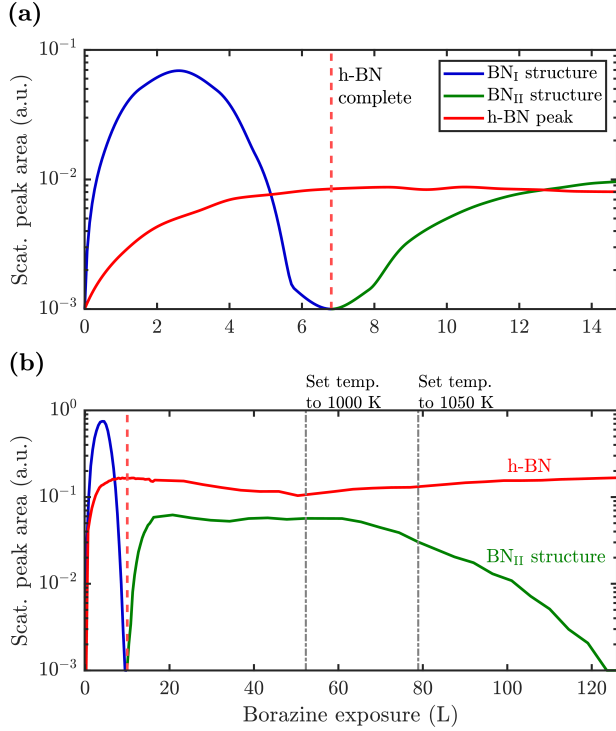


Figure 5: Peak areas of the characteristic diffraction peaks representing the different structures versus borazine exposure. After the BN_I structure has disappeared the h-BN peak saturates giving rise to a conversion and further exposure leads to the rise of the BN_II structure. Due to a higher substrate temperature of 915 K in (a), the BN_I structure disappears already after an exposure of ≈ 7 L compared to 10 L at 880 K in (b), thus indicating a kinetically driven conversion. Dosing in (b) is then further continued with subsequent changes of the surface temperature as stated above the diagram. After long enough exposure the BN_II structure disappears leaving a strong h-BN intensity behind.

kinetic barriers which need to be overcome in order to form ordered structures on the Ru substrate: A temperature of 750 K is necessary for the precursor structure to result, while at 880 K the h-BN formation sets in. As mentioned above, the BN_I precursor structure is always present, however, with increasing temperature its transformation into h-BN becomes faster.

As further illustrated in h-BN periodicity in the SI, the h-BN periodicity and superstructure are strongly dependent on the experimental parameters, in particular the growth temperature. The exact h-BN periodicity and the Moiré pattern upon h-BN formation on Ru(0001)^{23,25}, due to the small lattice mismatch between $a_{\text{h-BN}}$ and $a_{\text{Ru(0001)}}$, is determined by the growth temperature due to a so-called “lock-in” effect at that respective growth temperature⁷⁰. Together with the above reported additional structures, it confirms the complexity of the whole system and its dependence on minute changes of the growth parameters.

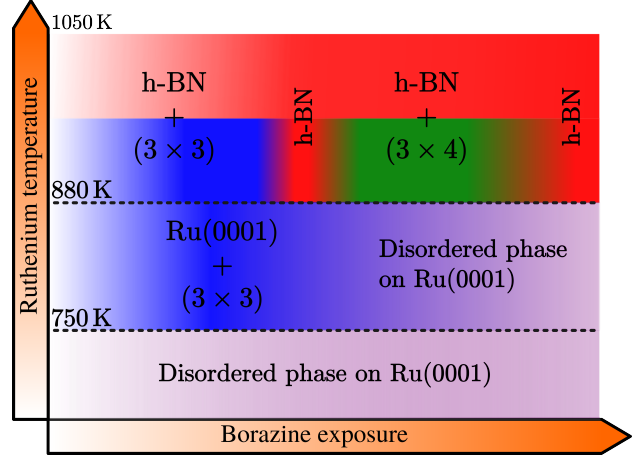


Figure 6: Schematic growth diagram of the different BN structures observed on a Ru surface within various temperature ranges and with increasing borazine exposure. At temperatures below 750 K no periodic structure is formed, while above, a (3×3) pattern is observed, disappearing again at higher exposures. Above 880 K the (3×3) structure precedes the growth of h-BN, with the temperature being necessary for the formation of h-BN. With increasing borazine exposure, the latter is followed by a structure with (3×4) periodicity with respect to the Ru lattice, leading again to h-BN after long enough exposure. (See text for a precise explanation of the structures.)

Discussion and summary

In summary, we investigated the growth of h-BN on a Ru(0001) substrate using helium atom scattering. Employing various growth conditions, characteristic periodic structures are measured during borazine exposure in addition to the h-BN diffraction peak as outlined in the diagram of Figure 6. Between 750 and 880 K a structure with (3×3) periodicity, that precedes the growth of h-BN, is observed with the minimum temperature necessary to form a h-BN overlayer being 880 K. Above this temperature, in addition to the emerging h-BN layer, we observe additional structures with a (3×3) superstructure followed by a (3×4) diffraction pattern, eventually disappearing and leaving a complete h-BN overlayer behind.

It is clearly evident from our observations that a precursor structure precedes the growth of h-BN at lower temperatures and an additional structure co-exists with h-BN at higher temperatures. Both are strongly dependent on the growth conditions, but always transform into a fully h-BN covered substrate at sufficiently high temperatures, thus confirming that the latter is the thermodynamically most stable structure. Our study of the structural evolution during the arrangement of h-BN from the precursor gas illustrates steps in the formation process itself and we hope to encourage future studies linking our structural information with chemical characterisation.

We believe that these intermediate metastable struc-

tures may be present in many more systems where 2D materials are grown based on precursor-based CVD, at least at lower temperatures and for higher amounts of excess hydrogen compared to the “ideal” growth conditions (see Outlook for other 2D materials in the supplementary information). In the case studied here, they ultimately always transform into the complete 2D layer - and thus usually higher temperatures are reported as the “ideal” growth conditions for h-BN in the literature.

These intermediate structures seem to have been largely overlooked so far. Possibly, because they are difficult to detect owing to experimental complications since the structural advent of 2D materials is often not investigated during the growth itself, or is only accessible *ex situ*. More importantly, with increasing growth temperature the transformation to h-BN may occur so fast that they are easily missed.²⁶

The strong dependence regarding the emergence of these structures on temperature and exposure suggests that further uncovered “routes” and polymerisation steps are viable and the system may present an ideal playground to end up with different nanostructures. It further suggests that a careful tuning of the growth conditions via temperature and excess hydrogen from the precursor may provide new broadly applicable strategies for controlling the growth of specific nanostructures. Additional possibilities involve changing the substrate or the precursor gas, and hence tuning the thermochemistry of the surface-adsorbate complex which may further alter the subsequent reaction pathway. E.g. by changing the substrate, the metal-N bond strength may be tuned since one expects the bonding strength to increase as one moves from right to left in the transition metal series. We hope that the wide ranging implications for a controlled growth of 2D materials and nanostructures will stimulate a broad range of new research, understanding and application.

Conflicts of interest

The authors declare no competing financial interest.

Acknowledgements

This research was funded in whole, or in part, by the Austrian Science Fund (FWF) [P29641-N36 & P34704-N]. For the purpose of open access, the author has applied a CC BY public copyright licence to any Author Accepted Manuscript version arising from this submission. We would also like to thank W. Allison for helpful discussion regarding the interpretation of the data, Chris Pickard for additional structure calculations based on a neural network approach and Moritz Will for his advice in terms of the precursor (bo-razine) purchase and treatment. A. R. acknowledges

funding by the Doctoral School and a scholarship of TU Graz. The authors acknowledge use of facilities at and support by the Cambridge Atom Scattering Centre (<https://atomscattering.phy.cam.ac.uk>) and the EPSRC award EP/T00634X/1 with the help of J. Ellis. M.S. is grateful for support from the Royal Society (URF/R/191029) and funding through the EPSRC (EP/S029834/1). This work used the ARCHER2 UK National Supercomputing Service (<http://www.archer2.ac.uk>) via membership of the UK's HEC Materials Chemistry Consortium, which is funded by the EPSRC (EP/R029431).

Supplemental information

Supplementary material can be found online.

Data availability

The datasets generated and analysed during the current study are available from the [TU Graz repository](#), with the identifier [10.3217/n9db1-sf358](#).

References

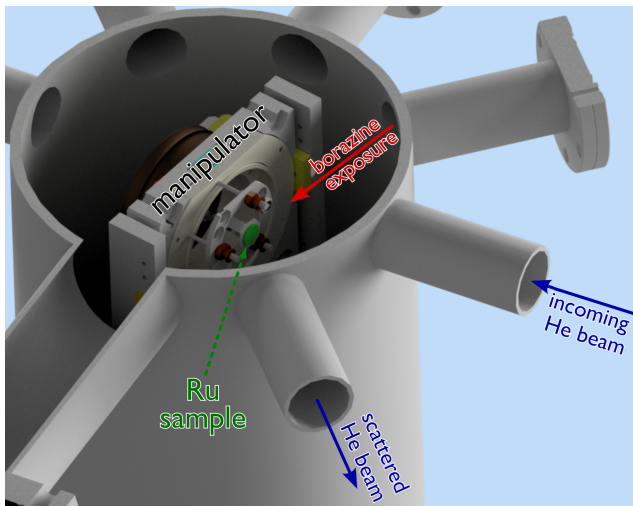
- (1) C. Anichini, W. Czepa, D. Pakulski, A. Aliprandi, A. Ciesielski and P. Samori, *Chem. Soc. Rev.*, 2018, **47**, 4860–4908.
- (2) H. X. Jiang and J. Y. Lin, *Semicond. Sci. Technol.*, 2014, **29**, 084003.
- (3) K. Y. Ma, L. Zhang, S. Jin, Y. Wang, S. I. Yoon, H. Hwang, J. Oh, D. S. Jeong, M. Wang, S. Chatterjee, G. Kim, A.-R. Jang, J. Yang, S. Ryu, H. Y. Jeong, R. S. Ruoff, M. Chhowalla, F. Ding and H. S. Shin, *Nature*, 2022, **606**, 88–93.
- (4) A. Zavabeti, A. Jannat, L. Zhong, A. A. Haidry, Z. Yao and J. Z. Ou, *Nano-Micro Lett.*, 2020, **12**, 66.
- (5) K. Zhang, Y. Feng, F. Wang, Z. Yang and J. Wang, *J. Mater. Chem. C*, 2017, **5**, 11992–12022.
- (6) W. Auwärter, *Surf. Sci. Rep.*, 2019, **74**, 1–95.
- (7) M. Jana and R. N. Singh, *Int. Mater. Rev.*, 2018, **63**, 162–203.
- (8) P. J. Fazen, E. E. Remsen, J. S. Beck, P. J. Carroll, A. R. McGhie and L. G. Sneddon, *Chem. Mater.*, 1995, **7**, 1942–1956.
- (9) Y. Shi, C. Hamsen, X. Jia, K. K. Kim, A. Reina, M. Hofmann, A. L. Hsu, K. Zhang, H. Li, Z.-Y. Juang, M. S. Dresselhaus, L.-J. Li and J. Kong, *Nano Lett.*, 2010, **10**, 4134–4139.
- (10) S. Bernard and P. Miele, *Materials Today*, 2014, **17**, 443–450.
- (11) S. Bernard, C. Salameh and P. Miele, *Dalton Trans.*, 2016, **45**, 861–873.
- (12) A. Talyzin, S. Luzan, K. Leifer, S. Akhtar, J. Fetzer, F. Cataldo, Y. Tsybin, C.-W. Tai, A. Dzwilewski and E. Moons, *J. Phys. Chem. C*, 2011, **115**, 13207–13214.
- (13) J. Li, E. Croiset and L. Ricardez-Sandoval, *Phys. Chem. Chem. Phys.*, 2014, **16**, 2954–2961.
- (14) H. Chen, W. Zhu and Z. Zhang, *Phys. Rev. Lett.*, 2010, **104**, 186101.
- (15) L. Wang, R. Lai, L. Zhang, M. Zeng and L. Fu, *ACS Materials Lett.*, 2022, **4**, 528–540.
- (16) M. Losurdo, M. M. Giangregorio, P. Capezzuto and G. Bruno, *Phys. Chem. Chem. Phys.*, 2011, **13**, 20836–20843.
- (17) X. Zhang, L. Wang, J. Xin, B. I. Yakobson and F. Ding, *J. Am. Chem. Soc.*, 2014, **136**, 3040–3047.
- (18) G. Lu, T. Wu, Q. Yuan, H. Wang, H. Wang, F. Ding, X. Xie and M. Jiang, *Nat. Commun.*, 2015, **6**, 6160.

- (19) J.-H. Choi, P. Cui, W. Chen, J.-H. Cho and Z. Zhang, *WIREs Comput Mol Sci*, 2017, **7**, e1300.
- (20) Z. Qiu, P. Li, Z. Li and J. Yang, *Acc. Chem. Res.*, 2018, **51**, 728–735.
- (21) M. R. Habib, T. Liang, X. Yu, X. Pi, Y. Liu and M. Xu, *Rep. on Prog. Phys.*, 2018, **81**, 036501.
- (22) H. Li, H. Zhu and R. Zhao, *New J. Chem.*, 2022, –.
- (23) A. Goriachko, He, M. Knapp, H. Over, M. Corso, T. Brugger, S. Berner, J. Osterwalder and T. Greber, *Langmuir*, 2007, **23**, 2928–2931.
- (24) S. Joshi, D. Eciya, R. Koitz, M. Iannuzzi, A. P. Seitsonen, J. Hutter, H. Sachdev, S. Vijayaraghavan, F. Bischoff, K. Seufert, J. V. Barth and W. Auwärter, *Nano Lett.*, 2012, **12**, 5821–5828.
- (25) J. Lu, P. S. E. Yeo, Y. Zheng, H. Xu, C. K. Gan, M. B. Sullivan, A. Castro Neto and K. P. Loh, *J. Am. Chem. Soc.*, 2013, **135**, 2368–2373.
- (26) D. Steiner, F. Mittendorfer and E. Bertel, *ACS Nano*, 2019, **13**, 7083–7090.
- (27) F. Müller, S. Hüfner and H. Sachdev, *Surf. Sci.*, 2009, **603**, 425–432.
- (28) D. Martoccia, T. Brugger, M. Björck, C. Schlepütz, S. Pauli, T. Greber, B. Patterson and P. Willmott, *Surf. Sci.*, 2010, **604**, L16–L19.
- (29) F. Orlando, P. Lacovig, L. Omiciuolo, N. G. Apostol, R. Larciprete, A. Baraldi and S. Lizzit, *ACS Nano*, 2014, **8**, 12063–12070.
- (30) J. Kelsall, P. S. M. Townsend, J. Ellis, A. P. Jardine and N. Avidor, *Phys. Rev. Lett.*, 2021, **126**, 155901.
- (31) D. Farias and K.-H. Rieder, *Rep. Prog. Phys.*, 1998, **61**, 1575.
- (32) J. Braun, J. P. Toennies and C. Wöll, *Phys. Rev. B*, 1999, **60**, 117075.
- (33) E. M. McIntosh, J. Ellis, A. P. Jardine, P. Licence, R. G. Jones and W. Allison, *Chem. Sci.*, 2014, **5**, 667.
- (34) B. Borca, S. Barja, M. Garnica, M. Minniti, A. Politano, J. M. Rodríguez-García, J. J. Hinarejos, D. Fariás, A. L. V. d. Parga and R. Miranda, *New J. Phys.*, 2010, **12**, 093018.
- (35) A. Tamtögl, E. Bahn, J. Zhu, P. Fouquet, J. Ellis and W. Allison, *J. Phys. Chem. C*, 2015, **119**, 25983–25990.
- (36) G. Anemone, E. Climent-Pascual, H. K. Yu, A. Al Taleb, F. Jiménez-Villacorta, C. Prieto, A. M. Wodtke, A. De Andrés and D. Fariás, *RSC Adv.*, 2016, **25**, 21235.
- (37) K. D. Gibson and S. J. Sibener, *J. Phys. Chem. C*, 2016, **120**, 24158–24164.
- (38) A. A. Taleb, G. Anemone, R. Miranda and D. Fariás, *2D Mater.*, 2018, **5**, 045002.
- (39) M. T. Paffett, R. J. Simonson, P. Papin and R. T. Paine, *Surf. Sci.*, 1990, **232**, 286–296.
- (40) F. Orlando, R. Larciprete, P. Lacovig, I. Boscarato, A. Baraldi and S. Lizzit, *J. Phys. Chem. C*, 2012, **116**, 157–164.
- (41) A. Farkas, P. Török, F. Solymosi, J. Kiss and Z. Kónya, *Appl. Surf. Sci.*, 2015, **354**, 367–372.
- (42) J.-W. He and D. W. Goodman, *Surf. Sci.*, 1990, **232**, 138–148.
- (43) L. Haug, J. P. Roth, M. Thaler, D. Steiner, A. Menzel, S. Tosoni, G. Pacchioni and E. Bertel, *Phys. Chem. Chem. Phys.*, 2020, **22**, 11704–11712.
- (44) F. Späth, J. Gebhardt, F. Düll, U. Bauer, P. Bachmann, C. Gleichweit, A. Görling, H.-P. Steinrück and C. Papp, *2D Mater.*, 2017, **4**, 035026.
- (45) M. Kim, S. W. Moon, G. Kim, S. I. Yoon, K. Kim, S. K. Min and H. S. Shin, *Chem. Mater.*, 2020, **32**, 4584–4590.
- (46) J. Lau, I. Calvo-Almazán, P. Townsend, D. Ward, A. Jardine, W. Allison, J. Ellis, B. Hinch and N. Avidor, *J. Phys. Chem. C*, 2018, **122**, 8941–8945.
- (47) N. Avidor, H. Hedgeland, G. Held, A. Jardine, W. Allison, J. Ellis, T. Kravchuk and G. Alexandrowicz, *J. Phys. Chem. A*, 2011, **115**, 7205–7209.
- (48) P. Kraus, C. Gösweiner, A. Tamtögl, F. Apolloner and W. E. Ernst, *EPL (Europhysics Letters)*, 2016, **114**, 56001.
- (49) E. Bahn, A. Tamtögl, J. Ellis, W. Allison and P. Fouquet, *Carbon*, 2017, **114**, 504–510.
- (50) N. Avidor and W. Allison, *J. Phys. Chem. Lett.*, 2016, **7**, 4520–4523.
- (51) C. Lin, G. Corem, O. Godsi, G. Alexandrowicz, G. R. Darling and A. Hodgson, *J. Am. Chem. Soc.*, 2018, **140**, 15804–15811.
- (52) A. Tamtögl, M. Sacchi, N. Avidor, I. Calvo-Almazán, P. S. M. Townsend, M. Bremholm, P. Hofmann, J. Ellis and W. Allison, *Nat. Commun.*, 2020, **11**, 278.
- (53) A. Tamtögl, A. Ruckhofer, D. Campi, M. Bremholm, W. E. Ernst, P. Hofmann and W. Allison, *Phys. Chem. Chem. Phys.*, 2021, **23**, 7637–7652.
- (54) A. Tamtögl, E. Bahn, M. Sacchi, J. Zhu, D. J. Ward, A. P. Jardine, S. J. Jenkins, P. Fouquet, J. Ellis and W. Allison, *Nat. Commun.*, 2021, **12**, 3120.
- (55) C.-Y. Lin, C.-E. Cheng, S. Wang, H. W. Shiu, L. Y. Chang, C.-H. Chen, T.-W. Lin, C.-S. Chang and F. S.-S. Chien, *J. Phys. Chem. C*, 2015, **119**, 12910–12915.
- (56) G. Benedek and J. P. Toennies, *Atomic Scale Dynamics at Surfaces*, Springer Berlin Heidelberg, 2018.
- (57) A. Jardine, H. Hedgeland, G. Alexandrowicz, W. Allison and J. Ellis, *Prog. Surf. Sci.*, 2009, **84**, 323–379.
- (58) G. Alexandrowicz and A. P. Jardine, *J. Phys.: Condens. Matter*, 2007, **19**, 305001.
- (59) B. Holst, G. Alexandrowicz, N. Avidor, G. Benedek, G. Bracco, W. E. Ernst, D. Fariás, A. P. Jardine, K. Lefmann, J. R. Manson, R. Marquardt, S. M. Artés, S. J. Sibener, J. W. Wells, A. Tamtögl and W. Allison, *Phys. Chem. Chem. Phys.*, 2021, **23**, 7653–7672.
- (60) P. Feulner and D. Menzel, *Surf. Sci.*, 1985, **154**, 465–488.
- (61) P. Sutter, R. Cortes, J. Lahiri and E. Sutter, *Nano Lett.*, 2012, **12**, 4869–4874.
- (62) J. Yin, J. Li, Y. Hang, J. Yu, G. Tai, X. Li, Z. Zhang and W. Guo, *Small*, 2016, **12**, 2942–2968.
- (63) C. Zhang, S. Zhao, C. Jin, A. L. Koh, Y. Zhou, W. Xu, Q. Li, Q. Xiong, H. Peng and Z. Liu, *Nat. Commun.*, 2015, **6**, 6519.
- (64) A. Kutana, A. Goriachko, Z. Hu, H. Sachdev, H. Over and B. I. Yakobson, *Adv. Mater. Interfaces*, 2015, **2**, 1500322.
- (65) M. Petrović, U. Hagemann, M. Horn-von Hoegen and F.-J. Meyer zu Heringdorf, *Appl. Surf. Sci.*, 2017, **420**, 504–510.
- (66) P. R. Kidambi, R. Blume, J. Kling, J. B. Wagner, C. Baehtz, R. S. Weatherup, R. Schloegl, B. C. Bayer and S. Hofmann, *Chem. Mater.*, 2014, **26**, 6380–6392.
- (67) L. Song, L. Ci, H. Lu, P. B. Sorokin, C. Jin, J. Ni, A. G. Kvashnin, D. G. Kvashnin, J. Lou, B. I. Yakobson and P. M. Ajayan, *Nano Lett.*, 2010, **10**, 3209–3215.
- (68) N. Guo, J. Wei, L. Fan, Y. Jia, D. Liang, H. Zhu, K. Wang and D. Wu, *Nanotechnology*, 2012, **23**, 415605.
- (69) S. M. Gilbert, T. Pham, M. Dogan, S. Oh, B. Shevitski, G. Schumm, S. Liu, P. Ercius, S. Aloni, M. L. Cohen and A. Zettl, *2D Mater.*, 2019, **6**, 021006.
- (70) D. Martoccia, S. Pauli, T. Brugger, T. Greber, B. Patterson and P. Willmott, *Surf. Sci.*, 2010, **604**, L9–L11.

Supplementary Information for Evolution of ordered nanoporous phases during h-BN growth: Controlling the route from gas-phase precursor to 2D material by *in-situ* monitoring.

Experimental Section

All measurements were performed with the ^3He spin echo apparatus at the [Cambridge Atom Scattering Centre](#). A schematic of the scattering chamber in the experimental setup is shown in Supplementary Figure 1. The helium beam is produced by supersonic expansion of ^3He gas through a nozzle and enters the scattering chamber through a series of differential pumping stages. The incident helium beam is scattered off the sample, which is, together with a sample holder, mounted on a 6-axis manipulator.¹ Atoms travelling in a particular outgoing direction pass along the second arm of the instrument, at 44.4° total scattering angle, and are then ionised and counted in a high sensitivity mass-spectrometer detector. The incidence angle, ϑ_i , with respect to the surface normal, can be varied to control the momentum transfer on scattering. The



Supplementary Figure 1: Schematic of the experimental setup in the helium scattering chamber. The incoming He beam is scattered off the ruthenium (Ru) sample in a fixed source-detector configuration with an angle of 44.4° . The sample is mounted onto a 5-axis manipulator and can be exposed to borazine via dosing thorough a leak valve.

Ru sample can be heated radiatively and by electron-bombardment from backside of the crystal and cooled via a thermal connection to a liquid nitrogen reservoir. The entire beamline is held at high vacuum to avoid any attenuation of the helium beam, and the sample and detector chamber require ultra high vacuum levels to maintain cleanness of the sample and a low ^3He background. The dosing was performed by backfilling the scattering chamber with borazine vapour, with borazine as provided by Katchem. To monitor the dosing rates, the chamber pressure was monitored, with typi-

cal overpressures between 1×10^{-9} and 5×10^{-8} mbar. At stages where borazine was not used for dosing the container was held at temperatures below 0°C .

The Ru(0001) surface was cleaned by Ar-sputtering and annealing to 1300 K with subsequent O_2 treatment to not less than 20 L at 700 K. The adsorbed O_2 was removed by repeated flashing cycles to 1200 K. The cleanliness of the sample was determined by helium reflectivity measurements and diffraction scans to show no features of adsorbed species. After reaching reflectivities of $\approx 23\%$ the sample was ready for the various dosing conditions. h-BN overlayers were removed by oxygen treatment at a sample temperature of 900 K, followed by the cleaning explained above. Borazine was supplied to the sample by backfilling the chamber through a leak-valve with typical overpressures between 1×10^{-9} and 5×10^{-8} mbar.

Computational Methods

For the DFT calculations we employed CASTEP,² a plane wave periodic boundary condition code. The plane wave basis set was truncated at an electron energy cut-off of 400 eV and we employ Vanderbilt ultrasoft pseudopotentials.³ The Brillouin zone was sampled with a $(4 \times 4 \times 1)$ Monkhorst-Pack k -point mesh.⁴ The Perdew Burke Ernzerhof exchange correlation functional⁵ was applied in combination with the Tkatchenko and Scheffler dispersion correction method.⁶ The Ru(0001) surface was modelled by a 5-layer slab in a (3×3) supercell, and an additional 15 \AA vacuum layer for separating the periodically repeated supercells in the z -direction. Positions of the atoms in the adsorbate and in the top three layers of the Ru substrate were left fully unconstrained. For the structural optimisations, the force tolerance was set to 0.05 eV/\AA .

The adsorption energies E_{ads} are defined to be:

$$E_{\text{ads}} = E_{\text{tot}}(x + ny) - E_{\text{tot}}(x) - nE_{\text{tot}}(y)$$

where $E_{\text{tot}}(x + ny)$ is the total energy of the system, $E_{\text{tot}}(x)$ is the energy of the substrate, $E_{\text{tot}}(y)$ is the energy of the adsorbate and n is the number of adsorbed molecules. The more negative E_{ads} , the more thermodynamically favourable it is for the species to adsorb.

In order to compare the intermediate structures with a different number of atoms we calculate the binding energy E_{bin} relative to Ru(0001) + 3 borazine molecules (3 borazine molecules are needed to form h-BN on a (3×3) cell) by appropriately adding or subtracting the energy of H_2 and borazine in the gas

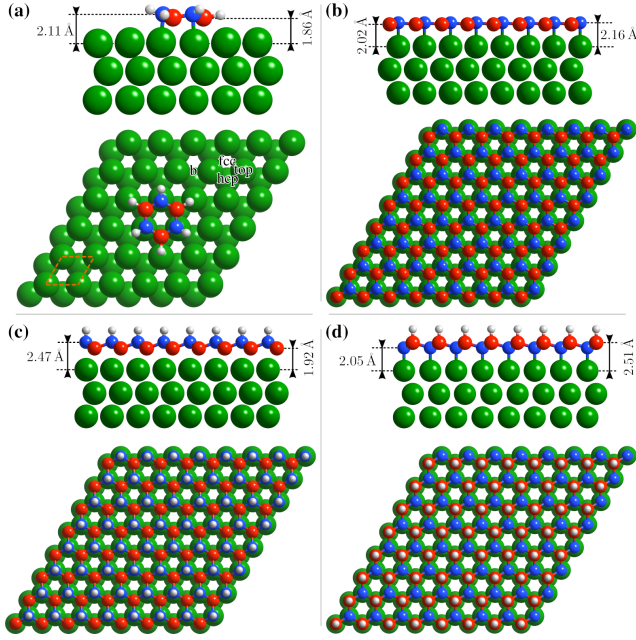
phase, to preserve stoichiometry:

$$E_{\text{bin}} = E_{\text{tot}} + \frac{n_{\text{H}}}{2} E_{\text{tot}}(\text{H}_2) + n_{\text{BZ}} E_{\text{tot}}(\text{BZ}) - E_{\text{tot}}(\text{Ru}) - E_{\text{tot}}(3\text{BZ})$$

where E_{tot} is the total energy of the system, $E_{\text{tot}}(\text{H}_2)$ and $E_{\text{tot}}(\text{BZ})$ are the energies of H_2 and borazine which remain in the gas phase, respectively and $E_{\text{tot}}(\text{Ru})$ and $E_{\text{tot}}(3\text{BZ})$ are the total energies of pristine Ru(0001) and 3 borazine molecules in the gas phase. The more negative E_{bin} , the stronger the binding and it becomes thermodynamically more favourable for the species to form.

Supplementary DFT calculations

The energetically most favourable adsorption site for a single intact borazine molecule per (3×3) supercell according to DFT calculations is shown in Supplementary Figure 2(a). The adsorption sites (top, hcp, fcc, b) are given relative to the centre of the borazine molecule. In



Supplementary Figure 2: (a) depicts the outcome of vdW-corrected DFT calculations for one borazine molecule ($\text{B}_3\text{N}_3\text{H}_6$) on Ru(0001), with the most favourable adsorption site being the fcc position. All possible adsorption sites are given with their according labels. (b) shows the top and side-view of h-BN on Ru(0001) with the corresponding interatomic distances. In (c) and (d) the optimised geometry for three partially dehydrogenated borazine molecules is illustrated, which essentially forms a hydrogenated version of h-BN/Ru(0001). Here (c) represents a “local” minimum as also seen from Supplementary Table 2. The hydrogen atoms stick out of the surface, yielding a high corrugation and hence the buckling will be different once the structure is dehydrogenated, such as for a complete h-BN layer with its corrugation reflecting the Moiré pattern.

addition to the calculations for one borazine molecule given in the main text we show the results for the

intact and partly dehydrogenated molecule with an initial rotation of 0° in Supplementary Table 1. When comparing the results we now see that in this case the hcp site is energetically most favourable with an adsorption energy of $E_{\text{ads}} = -8.85$ eV. If the borazine molecule is initially placed on a bridge site it undergoes a transition to the hcp position. Still, the results for the 60° rotation are energetically more favourable by ≈ 0.1 eV.

Supplementary Figure 2(c,d) shows that the outcome for calculations considering three partially dehydrogenated borazine molecules on Ru(0001), results in a structure similar to h-BN, except for the fact that the H atoms remain attached to the boron/nitrogen atoms. For comparison, Supplementary Figure 2(b) depicts the optimised structure for h-BN/Ru(0001).

Supplementary Table 2 illustrates that hydrogenation of the h-BN overlayer becomes thermodynamically unfavourable due to the correction with respect to molecular hydrogen in the gas phase and the high binding energy of the latter. The result is in line with hydrogenation experiments of metal supported h-BN, where atomic hydrogen exposure is required in order to facilitate the hydrogenation.⁷ Interestingly, in contrast to h-BN/Ni(111),⁷ H adsorption on top of the N-site is slightly more favourable than on top of the boron site for h-BN/Ru(0001) as can be seen from the adsorption energy per hydrogen atom.

Supplementary Table 1: DFT calculations for the adsorption structures of the borazine precursor on Ru(0001), based on a (3×3) supercell with one molecule per cell. The results are shown for an intact ($\text{B}_3\text{N}_3\text{H}_6$) and partially dehydrogenated ($\text{B}_3\text{N}_3\text{H}_3$) adsorbate, considering various initial adsorption sites and a rotation of 0° . The adsorption energies E_{ads} are given for the final optimised adsorption site and ΔE is the difference with respect to the minimum energy configuration of the system with the same dehydrogenation state.

$\text{B}_3\text{N}_3\text{H}_6$			$\text{B}_3\text{N}_3\text{H}_3$		
Site	E_{ads} (eV)	ΔE (eV)	Site	E_{ads} (eV)	ΔE (eV)
fcc	-1.28	2.80	fcc	-5.96	2.99
top	-1.21	2.87	top	-6.60	2.35
b→hcp	-3.99	0.08	b→hcp	-8.85	0.11
hcp	-3.99	0.08	hcp	-8.85	0.11

From the side view in Supplementary Figure 2(c,d) it becomes evident that the closest atom to the Ru substrate and the bond length change, depending whether nitrogen or boron remain hydrogenated. In Supplementary Figure 2(d) the hydrogen atoms appear to “pull” the boron away from the surface by 0.5 \AA and the sp^2 hybridised bonds to nitrogen gain more sp^3 character. Therefore the boron atom moves away from the surface to optimise these bonds, forming a tetra-

hedral (bond angle 106°). Likewise the nitrogen binds to the Ru orbitals, thus moving closer to the surface. If hydrogen desorbs from this structure pure h-BN is formed, as seen in Supplementary Figure 2(b). The boron-nitrogen bonds become stronger and therefore boron moves 0.5 \AA towards the Ru, to be in the same plane as the nitrogen. In addition the nitrogen orbitals are populated from the boron and the nitrogen-Ru interaction is weakened, resulting in a movement of the nitrogen atoms 0.11 \AA away from the Ru surface. For pure h-BN on Ru, the boron atoms are positioned only slightly lower than the nitrogen atoms (0.14 \AA). This may reflect the gain in stability from Ru-B bonding when boron is moved slightly into the hole site, compared to maintaining perfect sp^2 hybridised bonds.

Supplementary Table 2: DFT calculations for different configurations/structures with their respective energies.

Configuration	Adsorption energy per H atom (eV)	Adsorption site
hydrogenated h-BN/Ru	0.84	H on top of B
hydrogenated h-BN/Ru	0.81	H on top of N
Configuration	Physisorption energy (eV)	Stacking
h-BN on h-BN/Ru	-2.09	AB
Borazine on h-BN/Ru	-0.73	AB

As mentioned in the main text, we considered also borazine adsorption on top of h-BN/Ru as well as the formation of bi-layer h-BN. The physisorption energies are shown in the lower part of Supplementary Table 2, illustrating that both are thermodynamically favourable with a stronger physisorption energy for a second h-BN layer on top of h-BN/Ru. On the other hand, the corresponding binding energy for a single complete h-BN layer is -6.74 eV upon formation from 3 borazine molecules per supercell on Ru(0001). In the following we consider a possible route to the complete h-BN layer starting from the precursor structure as described in the main paper,

Supplementary Figure 3 shows the route through various steps based on DFT calculations. The first (precursor) structure is strongly bound with a binding energy E_{bind} (see Computational methods) of -6.28 eV in relation to the bare Ru surface and the molecules in the gas phase. The next step towards h-BN formation, involves dehydrogenation. The calculations show that if the three hydrogen atoms are detached only from the boron atoms they eventually reattach to the same boron sites. Therefore, initially the hydrogen atoms are

detached from the nitrogen atoms which adsorb on the Ru substrate within the nanopores, yielding a binding energy of -3.27 eV . At sufficient surface temperature eventually all hydrogen atoms will desorb from the surface yielding the third structure with a less favourable energy of 1.26 eV . If now the nanopore is filled with one additional borazine atom, h-BN is formed yielding the lowest binding energy (-6.74 eV). Therefore we conclude that the first structure is nearly as stable as h-BN and that on the route to h-BN several energy barriers have to be overcome. It should be mentioned however, that the calculations were performed at 0 K and that no entropy contributions were considered.

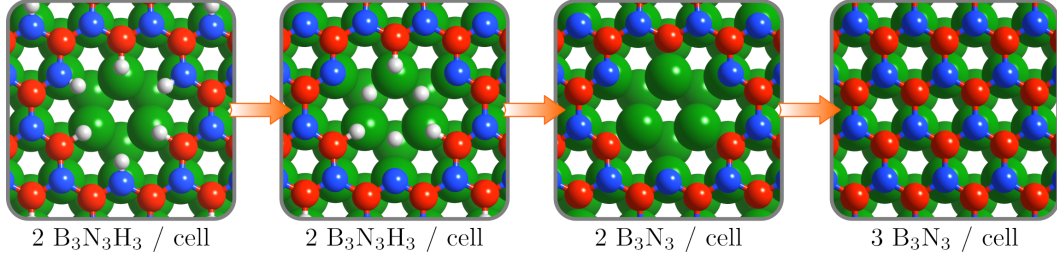
Supplementary diffraction scans

h-BN, sometimes also called “white graphene”, typically forms a Moiré pattern on the surfaces of reactive transition metals such as Rh(111) or Ru(0001), as mentioned in the main text. The two-dimensional h-BN layer on such surfaces exhibits periodic nanometric structures, often called “nanomesh”, with areas which are elevated from the surface, and areas closer to the surface. In Supplementary Figure 4 the characteristic diffraction pattern of the clean Ru sample (green) is compared to two overlayers on the same substrate.

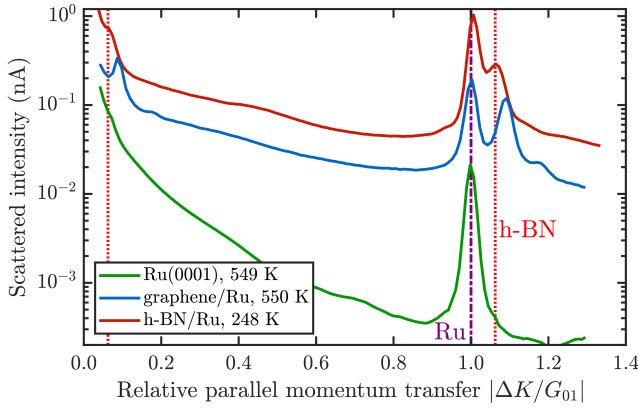
The scans of the single layer graphene and h-BN covered Ru show additional peaks close to the specular and first order Ru diffraction peaks. The blue curve depicts the scattering result for a graphene monolayer on Ru which has been studied extensively in earlier works.^{8,9} The graphene layer was grown by heating the Ru crystal to 1250 K for several minutes. Leaving the crystal at such high temperatures brings the carbon out of the bulk which then forms the honeycomb single layer graphene sheet. Graphene forms a (12-on-11) superstructure in which a (12×12) supercell of graphene coincides with a (11×11) supercell of ruthenium, giving rise to additional diffraction peaks at $|\Delta K/G_{01}| = 1/11 \equiv 0.09$ and $|\Delta K/G_{01}| = 12/11 \equiv 1.09$.

The diffraction pattern for h-BN on a Ru substrate is depicted in red in Supplementary Figure 4. Earlier works indicate that h-BN forms a (13-on-12) superstructure which can be identified by position of the diffraction peaks.¹⁰ Indeed the feature originating from the h-BN nanomesh to the right of the Ru diffraction peak shifts to smaller values of $|\Delta K/G_{01}|$ with respect to graphene, giving rise to a bigger supercell.

In Supplementary Figure 4 the scans for pure Ru and graphene were performed at a sample temperature of $T = 550 \text{ K}$ while the scan of h-BN was taken at 248 K . Due to thermal expansion it gives rise to a deviation of the position of the first order substrate (Ru) peak for the h-BN scan compared to the other two measurements as indicated by the purple line. In all scans the specular peak (at $|\Delta K/G_{01}| = 0$) was cut off due the high intensity and the first order diffraction



Supplementary Figure 3: Schematic of the possible route from the partially dehydrogenated precursor structure to h-BN via several intermediate structures based on vdW-corrected DFT calculations. As noted in the text, the precursor structure is already quite close to the binding energy for the complete h-BN layer. In contrast to the DFT calculations, where entropy contributions were not considered, additional dehydrogenation and bond breaking may occur due to the high experimental temperatures.



Supplementary Figure 4: Angular diffraction patterns using helium scattering. Comparison of the diffraction scans of the clean Ru(0001) surface (green), graphene on Ru (blue) and h-BN on Ru. The purple dash-dotted line indicates the first order diffraction position and the red dotted lines the h-BN reconstruction peaks.

peak of the Ru surface corresponds to $|\Delta K/G_{01}| = 1$.

In addition Supplementary Figure 4 clearly shows that the background intensity between the Ru diffraction peaks is much lower, indicating less inelastic scattering and fewer diffuse scattering when probing the clean Ru crystal. In both diffraction scans of h-BN and graphene the background increases by two orders of magnitude due to the increase of diffuse scattering. In addition, adlayers change the corrugation at the surface which is observed by the He atoms. X-ray studies showed that the peak-to-peak corrugation height of graphene is (0.82 ± 0.15) , whereas for the uppermost Ru-atomic layer it is (0.19 ± 0.02) .¹¹

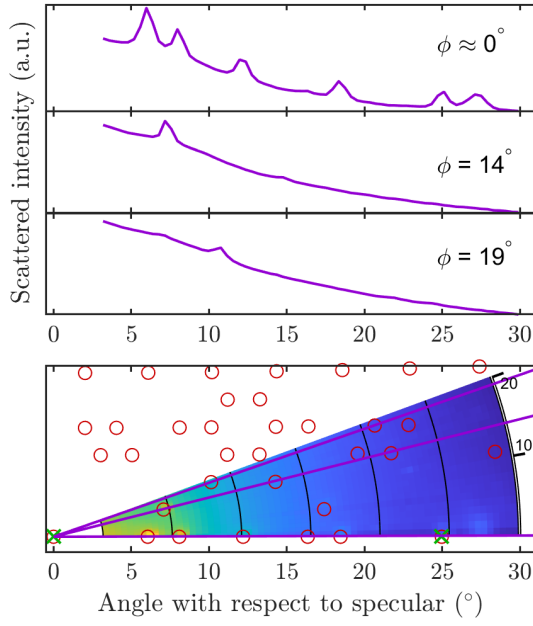
Performing a two-dimensional (2D) scan confirms that the diffraction peaks in the 1D angular diffraction scan of Figure 2(b) in the main text are correctly assigned to a (3×4) periodicity and cannot be explained as a subset of another periodicity or as domains with different rotations. Therefore we performed diffraction scans at various azimuthal orientations, since the BN_{II} structure has very distinct diffraction peaks in the high symmetry direction as well as along other azimuthal orientations. By rotation of the azimuthal angle of the

sample a 2D-plot in reciprocal space can be created (see Supplementary Figure 5). The green cross marks the Ru diffraction peak while the red circles indicate the calculated positions of the (3×4) structure peaks. In the top panel three exemplary diffraction scans at specific azimuthal angles φ are depicted. Small angles close to the specular peak are not shown due to their high intensity in all scans. The identification of the peaks verifies the assumption that the (3×4) structure is present in addition to the h-BN layer on the surface and cannot be explained e.g. as being part of another superstructure or rotated domains of a (3×3) structure.

h-BN periodicity and reconstruction

The h-BN periodicity and superstructure are strongly dependent on the experimental parameters, in particular the growth temperature. It is well known that h-BN forms a Moiré pattern on the Ru(0001) surface due to the small lattice mismatch between $a_{\text{h-BN}} = 2.505 \text{ \AA}$ and $a_{\text{Ru(0001)}} = 2.706 \text{ \AA}$.^{12,13} At room temperature, such a mismatch results in a superstructure where 13 unit cells of h-BN coincide with 12 unit cells of Ru: (13×13) on (12×12) . On the other hand, previous studies on a similar substrate showed that the h-BN overlayer and the substrate lock in at the temperature during the growth with the strong interlayer bonding causing the superstructure ratio to remain constant after cooling back down.¹⁴

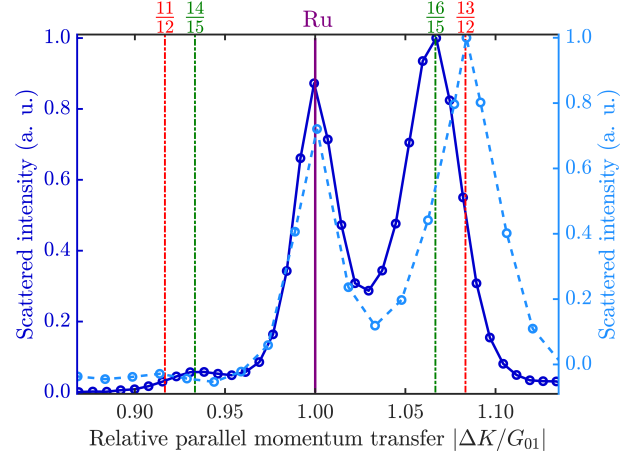
We show that the same holds for different growth temperatures of h-BN on Ru(0001). Detailed diffraction scans around the h-BN (01)-peak in Supplementary Figure 6 illustrate that for a h-BN synthesis at 1020 K (blue curve), the h-BN peak at $|\Delta K/G_{01}| = 1.067$ fits a superstructure ratio of 16/15 perfectly, as shown by the green vertical dash-dotted line. Upon growing the h-BN overlayer at a lower temperature of 900 K (cyan curve) the h-BN peak appears at a ratio of 13/12. The small peaks to the left of the first order Ru peak in Supplementary Figure 6 originate from the surface reconstruction with a 14/15 and 11/12 ratio, respectively. These reconstruction peaks can only arise



Supplementary Figure 5: 2-dimensional scan of the (3×4) structure of the adsorbed borazine molecules on the Ru surface. The polar plot consists of 22 individual logarithmic diffraction scans at various azimuthal orientations φ and a surface temperature of 300 K. The red circles indicate the calculated scattering positions for a (3×4) superstructure while the green crosses mark the Ru diffraction positions. Three exemplary scans at the top are drawn to elucidate the diffraction peak positions in dependence of φ .

if the system exhibits a true commensurate superstructure.^{14,15}

Our HAS measurements show a strong temperature dependence and thus a strong “lock-in” effect, as further discussed below. Compared to X-ray diffraction where a commensurate 14-on-13 superstructure was reported,¹⁶ we see that only h-BN growth at lower temperature (900 K with a borazine exposure of 15 L) followed by a slow subsequent cooling provides a 13 over 12 superstructure, similar to previous studies.¹⁷ After all, compared to the h-BN/Rh(111) system,¹⁸ the bonding strength of the N-atoms to the Ru substrate is predicted to increase and thus one expects a stronger “lock-in” effect on Ru as observed above. Moreover, due to HAS being strictly surface sensitive, our results can be interpreted as scattering that stems solely from the h-BN nanomesh while other methods may contain contributions from the substrate structure. E.g, a coincidental overlay of the flat h-BN monolayer on a completely flat Ru substrate would not give rise to a diffraction pattern as shown in Supplementary Figure 2(a) and Supplementary Figure 6. Together with the above reported additional structures, it confirms the complexity of the whole system and its dependence on minute changes of the growth parameters.



Supplementary Figure 6: Diffraction scans of the h-BN periodicity illustrate that the exact superstructure of the overlayer depends on the growth temperature, with the blue scan for h-BN grown at 1020 K and the dashed cyan curve for h-BN grown at 900 K. The h-BN peaks at the right-hand side of the Ru peak at $|\Delta K/G_{01}| = 1$ show, that h-BN adopts a larger superstructure with increasing growth temperature. Due to the decreasing lattice mismatch the overlayer adopts a 16/15 ratio versus a 13/12 ratio at 900 K. The “lock-in” effect (see text) is confirmed by the small (substrate) reconstruction peaks on the left-hand side. For better identification of the peaks a linear background was subtracted from the untreated data and the sample was subsequently cooled down to room temperature for the duration of the scan.

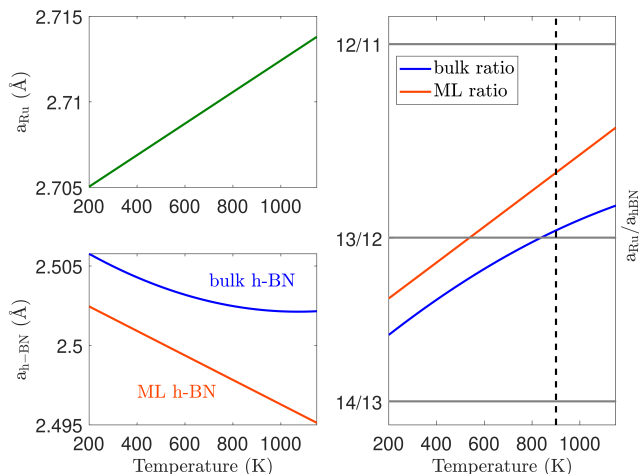
Looking at the thermal expansion coefficients of bulk h-BN and the Ru(0001) surface gives a rough estimation for the temperature at which the 13/12 superstructure is favourable. The thermal expansion of bulk h-BN¹⁹ and the Ru surface²⁰ are given by:

$$a_{\text{h-BN}} = 2.505 - 7.42 \times 10^{-6} \cdot (T - 297) + 4.79 \times 10^{-9} \cdot (T - 297)^2 \quad (1a)$$

$$a_{\text{Ru}} = 2.706 + 9.22 \times 10^{-6} \cdot (T - 293) \quad (1b)$$

Here the lattice constant for Ru $a_{\text{Ru}} = 2.706 \text{ \AA}$ was taken for a surface temperature of 293 K, with 297 K for $a_{\text{h-BN}}$, hence the subtraction of these values.

The Ru thermal expansion is depicted in the upper left panel of Supplementary Figure 7, while the slope of bulk h-BN is shown as a blue line in the lower left panel. In addition, the thermal expansion for a single monolayer (ML) of h-BN as calculated by Thomas *et al.*²¹ is drawn in orange. Taking the ratio of the values for h-BN and Ru then yields the expected superstructure at a given surface temperature, as shown in the right panel of Supplementary Figure 7. The expected fraction of 13/12 nicely fits the value of 900 K when using the bulk value of the thermal expansion.



Supplementary Figure 7: Thermal expansion for the Ru surface (upper left panel) and bulk h-BN as well as monolayer (ML) h-BN (lower left panel). The ratio of the Ru surface lattice constant and the h-BN lattice constant versus temperature (right panel) provides an estimate of the expected superstructure. The grey horizontal lines depict the respective superstructure ratios while the dashed vertical line indicates a growth temperature of 900 K.

Supplementary discussion

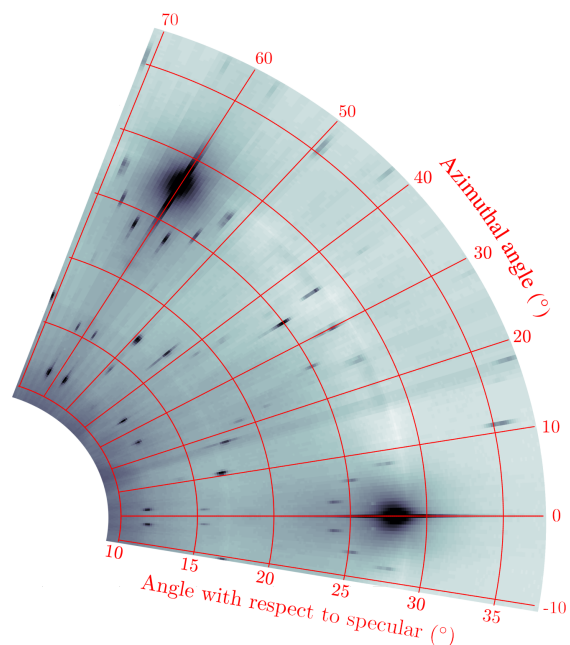
In the following we discuss further scenarios of the BN_{II} structure. As mentioned in the main text, the surface temperature strongly influences the kinetics and thus the duration and appearance of the additional superstructures. At temperatures above 1000 K the (3×4) structure (BN_{II}) slowly vanishes (see Figure 5 in the main text) which leads to the assumption that either strongly bound atoms/molecules desorb into the gas phase or convert into another structure. As mentioned earlier the dehydrogenation of borazine already starts at lower temperatures²² leading to the assumption that the adsorbed species on Ru(0001) are at least partly dehydrogenated.

In the following we provide several scenarios for the origin of the (3×4) structure and discuss their plausibilities. The results could be interpreted as if borazine converts upon adsorption to both h-BN and a (3×3) structure (BN_{I}). However, given the results which are reported in the main paper, it is clear that borazine only adsorbs in a (3×3) superstructure, and at 880 K a (relatively fast) conversion to h-BN occurs. The h-BN and BN_{I} structure grow together until the BN_{I} reservoir is depleted, and no more h-BN is created. At this point we can conclude that the (3×4) (BN_{II}) is not a precursor to h-BN and is also not converted from the BN_{I} structure. Since the (3×3) peaks degrade completely, the rise of the BN_{II} structure does not compete with the conversion of the BN_{I} structure to h-BN.

When looking at Figure 5 in the main paper one might also think that after the BN_{I} structure vanishes and the h-BN peak saturates, that the h-BN monolayer is complete and the additional borazine exposure

gives rise to a second layer being formed. This layer could consist of partly dehydrogenated borazine forming a periodic structure on top of the existing h-BN layer. According to literature, the CVD process for h-BN growth is usually considered to be self-terminating after a single layer, while some works also showed that multilayers are formed,²³ however, typically these require different growth approaches.^{24–27} As described in the main paper, from our experimental observations we can rule out the behaviour of multilayer h-BN growth and ascribed the BN_{II} structure to a second chemisorbed layer on top of h-BN.

Another possible scenario would be the growth of a superstructure in-between the already grown h-BN islands. As mentioned in the main manuscript an earlier work investigated the CVD growth of h-BN on Ir(111) and identified a (6×2) superstructure in-between the h-BN islands.²⁸ A similar behaviour could lead to the formation of a (3×4) structure in-between the h-BN islands on Ru. This intermediate structure eventually upon further borazine exposure converts into h-BN which connects the previously formed h-BN islands. However the areas which formed under this condition are less stable since they convert back to a (3×4) structure upon heating of the sample (see phenomenological cycle equation in the main paper). Upon further annealing of the surface the structures in-between the stable h-BN islands eventually desorb from the surface leaving behind some h-BN islands.



Supplementary Figure 8: A 2-dimensional diffraction scan of CVD-grown graphene on Ni(111) at temperatures below the “ideal” growth temperatures, reveals additional diffraction peaks which transform only upon heating to 730 K into the (1×1) graphene/Ni(111) structure.

Outlook for other 2D materials

We hope that our initial findings encourage future investigations to give insight on the peculiar intermediate structures during the CVD growth of h-BN on Ru(0001). In fact we note that there is some preliminary experimental evidence as shown in Supplementary Figure 8, that an intermediate / precursor structure exists also for CVD of graphene on Ni(111) at temperatures below the best growth conditions. Only upon heating to 730 K the additional diffraction peak vanishes, leaving just the (1×1) graphene/Ni(111) structure behind²⁹.

Supplementary References

- (1) A. Tamtögl, E. A. Carter, D. J. Ward, N. Avidor, P. R. Kole, A. P. Jardine, J. Ellis and W. Allison, *Rev. Sci. Instrum.*, 2016, **87**, 066108.
- (2) S. J. Clark, M. D. Segall, C. J. Pickard, P. J. Hasnip, M. I. J. Probert, K. Refson and M. C. Payne, *Z. Kristallogr. Cryst. Mater.*, 2009, **220**, 567–570.
- (3) D. Vanderbilt, *Phys. Rev. B*, 1990, **41**, 7892–7895.
- (4) H. J. Monkhorst and J. D. Pack, *Phys. Rev. B*, 1976, **13**, 5188–5192.
- (5) J. P. Perdew, K. Burke and M. Ernzerhof, *Phys. Rev. Lett.*, 1996, **77**, 3865–3868.
- (6) A. Tkatchenko and M. Scheffler, *Phys. Rev. Lett.*, 2009, **102**, 073005.
- (7) F. Späth, J. Gebhardt, F. Düll, U. Bauer, P. Bachmann, C. Gleichweit, A. Görling, H.-P. Steinrück and C. Papp, *2D Mater.*, 2017, **4**, 035026.
- (8) B. Borca, S. Barja, M. Garnica, M. Minniti, A. Politano, J. M. Rodriguez-García, J. J. Hinarejos, D. Fariás, A. L. V. d. Parga and R. Miranda, *New J. Phys.*, 2010, **12**, 093018.
- (9) D. Maccariello, D. Campi, A. Al Taleb, G. Benedek, D. Fariás, M. Bernasconi and Miranda, *Carbon*, 2015, **93**, 1–10.
- (10) D. Martoccia, T. Brugger, M. Björck, C. Schlepütz, S. Pauli, T. Greber, B. Patterson and P. Willmott, *Surf. Sci.*, 2010, **604**, L16–L19.
- (11) D. Martoccia, M. Björck, C. M. Schlepütz, T. Brugger, S. A. Pauli, B. D. Patterson, T. Greber and P. R. Willmott, *New Journal of Physics*, 2010, **12**, 043028.
- (12) W. Paszkowicz, J. B. Pelka, M. Knapp, T. Szyszko and S. Podsiadlo, *Appl. Phys. A*, 2002, **75**, 431–435.
- (13) J. W. Arblaster, *Platinum Metals Review*, 2013, **57**, 127–136.
- (14) D. Martoccia, S. Pauli, T. Brugger, T. Greber, B. Patterson and P. Willmott, *Surf. Sci.*, 2010, **604**, L9–L11.
- (15) N. Leconte and J. Jung, *2D Mater.*, 2020, **7**, 031005.
- (16) D. Martoccia, T. Brugger, M. Björck, C. Schlepütz, S. Pauli, T. Greber, B. Patterson and P. Willmott, *Surf. Sci.*, 2010, **604**, L16–L19.
- (17) A. Goriachko, He, M. Knapp, H. Over, M. Corso, T. Brugger, S. Berner, J. Osterwalder and T. Greber, *Langmuir*, 2007, **23**, 2928–2931.
- (18) R. Laskowski, P. Blaha and K. Schwarz, *Phys. Rev. B*, 2008, **78**, 045409.
- (19) R. S. Pease, *Acta Crystallographica*, 1952, **5**, 356–361.
- (20) E. Ferrari, L. Galli, E. Miniussi, M. Morri, M. Panighel, M. Ricci, P. Lacovig, S. Lizzit and A. Baraldi, *Phys. Rev. B*, 2010, **82**, 195420–.
- (21) S. Thomas, K. M. Ajith, S. Chandra and M. C. Valsakumar, *J. Phys.: Condens. Matter*, 2015, **27**, 315302–.
- (22) F. Orlando, R. Larciprete, P. Lacovig, I. Boscarato, A. Baraldi and S. Lizzit, *J. Phys. Chem. C*, 2012, **116**, 157–164.
- (23) P. R. Kidambi, R. Blume, J. Kling, J. B. Wagner, C. Baetz, R. S. Weatherup, R. Schloegl, B. C. Bayer and S. Hofmann, *Chem. Mater.*, 2014, **26**, 6380–6392.
- (24) A. A. Tonkikh, E. N. Voloshina, P. Werner, H. Blumtritt, B. Senkovskiy, G. Güntherodt, S. S. P. Parkin and Y. S. Dedkov, *Sci. Rep.*, 2016, **6**, 23547.
- (25) A.-R. Jang, S. Hong, C. Hyun, S. I. Yoon, G. Kim, H. Y. Jeong, T. J. Shin, S. O. Park, K. Wong, S. K. Kwak, N. Park, K. Yu, E. Choi, A. Mishchenko, F. Withers, K. S. Novoselov, H. Lim and H. S. Shin, *Nano Lett.*, 2016, **16**, 3360–3366.
- (26) N. Guo, J. Wei, L. Fan, Y. Jia, D. Liang, H. Zhu, K. Wang and D. Wu, *Nanotechnology*, 2012, **23**, 415605.
- (27) P. Sutter, J. Lahiri, P. Zahl, B. Wang and E. Sutter, *Nano Lett.*, 2013, **13**, 276–281.
- (28) M. Petrović, U. Hagemann, M. Horn-von Hoegen and F.-J. Meyer zu Heringdorf, *Appl. Surf. Sci.*, 2017, **420**, 504–510.
- (29) A. Tamtögl, E. Bahn, J. Zhu, P. Fouquet, J. Ellis and W. Allison, *J. Phys. Chem. C*, 2015, **119**, 25983–25990.